Journal of Materials Science & Technology 177 (2024) 234–245

Contents lists available at ScienceDirect

Journal of Materials Science & Technology

journal homepage: www.elsevier.com/locate/jmst

Research Article

Impact of uneven distribution of grain characteristics on yield strength and martensitic transformation of as-hot-rolled medium-entropy alloys

Jungwan Lee[a], Hyojin Park[a], Sujung Son[a], Jae Wung Bae[b,*], Jin You Kim[c], Sung Kyu Kim[c], Jae-il Jang[d], Hyoung Seop Kim[a,e,f,g,**]

[a] Department of Materials Science and Engineering, Pohang University of Science and Technology (POSTECH), Pohang 37673, Republic of Korea
[b] Department of Metallurgical Engineering, Pukyong National University, Busan 48513, Republic of Korea
[c] Technical Research Laboratories, Energy and Shipbuilding Steel Research Group, POSCO, Pohang, Republic of Korea
[d] Division of Materials Science and Engineering, Hanyang University, Seoul 04763, Republic of Korea
[e] Graduate Institute of Ferrous & Eco Materials Technology (GIFT), Pohang University of Science and Technology (POSTECH), Pohang 37673, Republic of Korea
[f] Center for Heterogenic Metal Additive Manufacturing, Pohang University of Science and Technology (POSTECH), Pohang 37673, Republic of Korea
[g] Advanced Institute for Materials Research (WPI-AIMR), Tohoku University, Sendai 980-8577, Japan

ARTICLE INFO

Article history:
Received 15 July 2023
Revised 7 September 2023
Accepted 7 September 2023
Available online 28 September 2023

Keywords:
Dynamic recrystallization
Nucleation and growth
Heterogeneity
Grain size distribution
Deformation-induced martensitic transformation

ABSTRACT

As-hot-rolled medium-entropy alloys (MEAs) with unevenly distributed grain sizes of face-centered cubic grains exhibit better yield strength without uniform elongation loss compared to cold-rolled and annealed ones. Successive operation of dynamic recrystallization (DRX) during several hot rolling passes leads to a wide range of grain sizes from submicrons to tens of micrometers due to the grain growth after nucleation: early recrystallized grains are coarser than recently recrystallized ones. Not only the grain size but internal dislocation density of the recently recrystallized grain is low. During the tensile deformation of the hot-rolled MEAs at −196 °C, dislocation pile-ups in the relatively soft and fine DRX grains enhance yield stress and hetero-deformation-induced strain hardening. Thanks to the enhanced yield stress of the as-hot-rolled MEAs, stress-induced martensitic transformation easily occurs. Notably, partially DRXed MEAs hot-rolled at 800 °C have lower yield stress than fully DRXed ones, hot-rolled at 900 and 1000 °C. This is attributed to the softening effect of the stress-induced body-centered cubic martensitic transformation in unrecrystallized coarse grains prior to the yielding, which lowers the yield stress of the partially DRXed ones. After yielding, the martensitic transformation facilitates strain hardening and early necking is precluded. This study presents a fresh outlook on the uneven distribution of grain sizes by hot rolling beneficial to mechanical responses of uniform elongation of ~45% despite the as-rolled states with an advantage of simplified thermo-mechanical processes.

1. Introduction

Multi-principal element alloys (MPEAs), which extend conventional alloying methods of adding various sub-elements to the main element, have been numerously investigated in the past decade [1–3]. The origin of the MPEAs began with an equiatomic CoCrFeMnNi alloy called high-entropy alloy (HEA) with the maximized configurational entropy of mixing in the five-element alloy system [4]. It presents various desirable physical properties, including tensile properties [1,5], fracture toughness [1,6], corrosion resistance [7], and antifouling properties [8], owing to four core effects of HEAs [9]. However, the goals of material properties are unlimited, so the efforts to achieve them always remain never-ending tasks for material scientists.

In order to upgrade the strength and price competitiveness of the MPEA, a kind of ferrous medium-entropy alloy (FeMEA) with an increased Fe content has been introduced with the conventional processes of cast, rolling, and annealing [10,11]. The lowered phase stability of face-centered cubic (FCC) matrix due to the increase in the Fe composition led to deformation-induced phase transformation to body-centered cubic (BCC) or/via hexagonal close-packed (HCP) phase by a quasi-static tensile test at liquid nitrogen tem-

* Corresponding author.
** Corresponding author at: Graduate Institute of Ferrous & Eco Materials Technology (GIFT), Pohang University of Science and Technology (POSTECH), Pohang 37673, Republic of Korea.
E-mail addresses: jwbae@pknu.ac.kr (J.W. Bae), hskim@postech.ac.kr (H.S. Kim).

https://doi.org/10.1016/j.jmst.2023.09.007
1005-0302/

perature [11]. The transformation-induced plasticity (TRIP) effectively increasing the mechanical properties has been widely studied throughout the synergetic strengthening mechanisms. For instance, the effects of precipitates [12] and elemental compositions of the MPEAs [10,11] on controlling the TRIP behavior and inhomogeneous grain size distribution from several nanometers to hundreds of micrometers by recently noted metal additive manufacturing (MAM) [13] are fairly high-profile studies. In particular, designing heterogeneous metallic materials induced by heterogeneities of grain sizes, crystal structures, and/or elemental distributions is one of the most promising microstructural design strategies for better mechanical performances [14–16]. The strengthening mechanism called hetero-deformation-induced (HDI) strengthening originates from high plastic incompatibility between relatively hard and soft domains [14–16]. On this wise, the research field of the MPEAs has expanded from homogeneous single phase to heterogeneous microstructures with the aid of phase transformation from the single phase. The heterogeneous microstructures were obtained by controlling the elemental composition of the MPEAs [14] and/or exploiting adequate alloy manufacturing processes [13,17].

In this regard, the MAM technologies effective in rendering hierarchically heterogeneous microstructures are currently leading the global manufacturing trend [13,17], whereas the heterostructuring strategies toward wrought materials are still limited. For example, pre-straining followed by heat treatment in TRIP-based MPEAs produces heterogeneous grain size distribution by reverse martensitic transformation, which in turn enhances the mechanical properties [18]. However, the overall processing history is substantially complicated and difficult to be applied industrially. Recently, partially recrystallized microstructures have been obtained by heat treatment of cold-rolled wrought MPEAs for a short time before full recrystallization occurred [19–21]. The heterogeneity of grain size distribution between recrystallized and unrecrystallized grains develops the strain gradients accommodated by the generation of geometrically necessary dislocations (GNDs), leading to a substantial increase in yield strength [19–21]. The studies of heterogeneous microstructures through partial recrystallization are fascinating, but it is questionable whether those can be widely applied from an industrial perspective because the annealing conditions satisfying the partial recrystallization are quite limited.

Here, we propose an efficient and simple thermo-mechanical processing route to obtain the heterogeneous microstructures in as-rolled wrought MPEAs by hot rolling in place of conventional cold rolling and annealing. $Fe_{60}Co_{15}Ni_{15}Cr_{10}$ (at.%) FeMEA utilizing the TRIP behavior [10,11] is considered as a good candidate material for applying the heterostructuring strategies in a bid to enhance the mechanical properties. The microstructural heterogeneity is based on several rounds of dynamic recrystallization (DRX) during the hot rolling. The DRX causes a wide range of grain sizes, spanning from submicrons to tens of micrometers. This variation is because the onset of DRX varies among grains, and subsequent grain growth occurs after nucleation during the hot rolling. In other words, the early recrystallized grains are coarser than the recently recrystallized ones. The heterogeneity of the grain size and high dislocation density in the as-rolled FeMEA result in enhanced yield strength and substantial ductility. Above all, the major findings of this study are: (i) exceptional uniform elongation of ~45% despite the as-rolled condition and (ii) anomalous hot rolling temperature dependence of the yield strength of the as-rolled FeMEAs stemming from temperature-dependent DRX behavior. Though the DRXed microstructures have been investigated in other MPEAs [22], to the best of our knowledge, the influence of the DRX structure on macroscopic mechanical responses such as the TRIP behavior is new-fangled. This treatise systematically characterizes the hot-rolled microstructures of the FeMEAs using electron backscatter diffraction (EBSD), electron channeling contrast imaging (ECCI), and transmission electron microscopy (TEM) and describes the corresponding remarkable tensile properties.

2. Experimental

2.1. Alloy fabrication and thermo-mechanical processes

Six ingots of the $Fe_{60}Co_{15}Ni_{15}Cr_{10}$ (at.%) FeMEAs were cast in dimensions of 50 mm × 35 mm × 7 mm by vacuum induction melting (MC100V, Indutherm) with a purity of more than 99.9% alloying element pellets. The as-cast ingots were homogenized at 1100 °C for 6 h followed by water quenching [10]. Three of the homogenized alloys were hot-rolled with a thickness reduction ratio of 78.6% from 7 mm to 1.5 mm at 800, 900, and 1000 °C, and then air quenched. Each rolling pass reduced the thickness by 15%, and whenever two rolling passes were repeated back and forth, the alloy was briefly reheated in the furnace for 5 min at each hot rolling temperature to prevent excessive grain coarsening [23,24]. These hot-rolled FeMEAs are denoted as HRs and specifically HR800, HR900, and HR1000 regarding the hot rolling temperatures. As a comparison group, the other homogenized FeMEAs were cold-rolled at room temperature with the same thickness reduction to 1.5 mm. For recrystallization, the cold-rolled FeMEAs were annealed at 800 °C for 10, 30, and 60 min followed by water quenching, denoted as CR-A810, CR-A830, and CR-A860, respectively. From here, the as-hot-rolled and as-annealed states are considered initial states prior to tensile tests.

2.2. Tensile tests and microstructure characterization

Rectangular dog-bone-shaped tensile specimens with a gage length of 5 mm along the rolling direction (RD) and width of 2.5 mm were sliced by electrical discharge machining from the middle part of the rolled plates with a thickness of 1.5 mm. Normal directional (ND) planes of the tensile samples on both sides were mechanically polished with SiC abrasive papers of 600, 800, and 1200 grit. For accurate elongations, two indentations were marked at the same interval of 5 mm on the tensile specimens using a Vickers hardness tester before the tensile tests. The tensile tests were carried out at liquid nitrogen temperature (−196 °C) using an Instron 1361 universal testing machine with an attached liquid nitrogen chamber. A constant strain rate was set as 10^{-3} s^{-1}. Each test was performed in triplicate to confirm the reproducibility of the tensile results.

To characterize the microstructural evolution by the tensile deformation, the initial and tensile deformed samples were mechanically polished up to 1200 grit SiC papers followed by electropolishing using a solution of 92% acetic acid + 8% perchloric acid at 9 V for 15 s. Multifarious microstructural analyses were performed by EBSD, ECCI, TEM, energy dispersive spectroscopy (EDS), X-ray diffraction (XRD), and convolutional multiple whole profile (CMWP) fitting. The EBSD and ECCI were conducted using a JSM-7900F scanning electron microscope. The EBSD images were scanned in the middle of transverse directional (TD) planes of the HRs and ND planes of the CR-A810 using an Oxford integrated AZtec*HKL* advanced EBSD system. The TD plane is beneficial for observing dislocation behavior such as shear bands in the as-rolled materials [20]. Each EBSD step size was 0.7 μm at a magnification of 180 × and some highly magnified images were scanned with nanometer-level step sizes, which are mentioned in the figure caption. Considering that the EBSD is not capable of monitoring the dislocation structures, the ECCI facilitates the observation of near-surface dislocations of an electropolished bulk metallic sample without any destructive sample preparation [25]. After the insertion of a backscattered electron detector, the sample

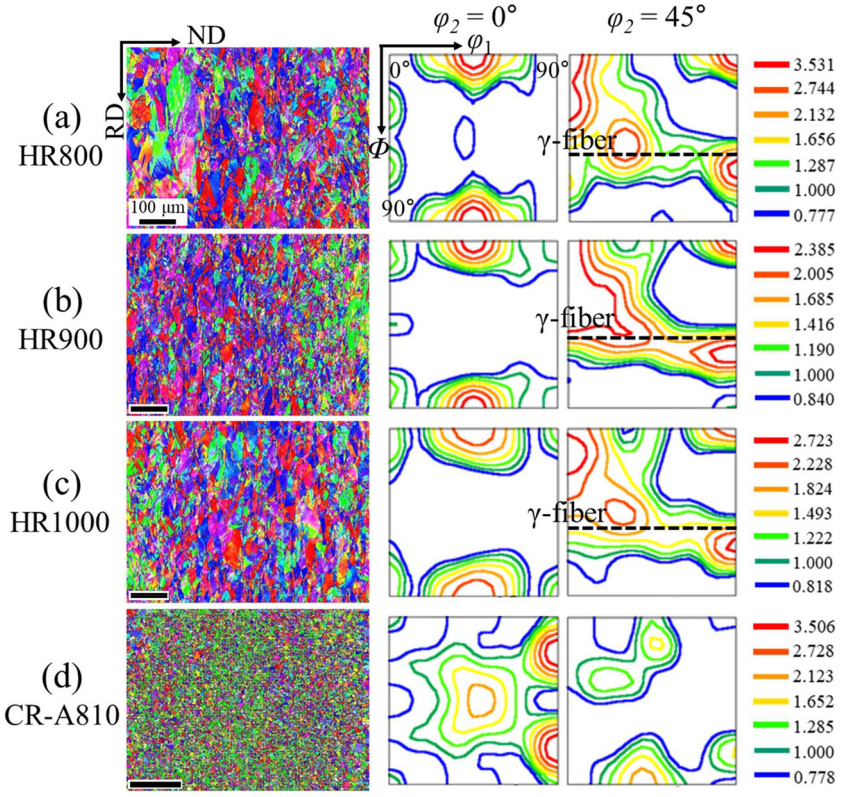

Fig. 1. Initial microstructures using EBSD. (a–c) HRs and (d) CR-A810 in IPF maps and ODF maps (scale bar, 100 μm).

was tilted from −2° to 2° toward the best quality of the ECC image at a working distance of 5.5 mm by an accelerating voltage of 20 kV. The samples for TEM analysis with a thickness of 70 nm were prepared using a dual-beam focused ion beam (FEI Helios 600) and investigated with JEM-2200FS. An EDS line profile was carried out to monitor whether atomic diffusion had occurred by the deformation-induced martensitic transformation (DIMT) during the tensile test at −196 °C.

The XRD analyses were performed on the HRs and CR-A810 with a Bruker D8 Advance diffractometer using Cu K_α radiation under the range of diffraction angle (2θ) from 30° to 100° with a step size of 0.013°. To calculate the dislocation density, a CMWP method was exploited based on the XRD profiles of the HRs and CR-A810 [26]. For the CMWP fitting, LaB6 (SRM 660c, NIST) as a standard material was used to deduct the instrumental effect of the X-ray diffractometer [26].

3. Results

3.1. DRXed microstructures of as-hot-rolled MEAs

The initial microstructures of the HRs and CR-A810 in a broad scope are displayed in Fig. 1. In an inverse pole figure (IPF) map of the HR800 in Fig. 1(a), coarse unrecrystallized grains elongated along the RD with grain sizes of a few hundred micrometers are observed, while the DRX grains are relatively fine. Prior to the hot rolling, the as-homogenized MEA had equiaxed grains with an average grain size of 189.5 ± 81.5 μm in Fig. S1 in Supplementary Information. The HR900 and HR1000 are fully DRXed with finer average grain sizes than that of the HR800: average grain sizes of 38.5 ± 40.5, 14.8 ± 10.6, and 22.8 ± 15.9 μm for the HR800, HR900, and HR1000, respectively (Fig. S2). The coarse unrecrystallized grains in the HR800 contribute to the largest mean grain size. The HR1000 has a larger average grain size than the HR900 because an increase in temperature activates grain growth. Moreover, given that the DRX occurs more prominently at higher rolling temperatures, it occurs earlier at 1000 °C than at 900 °C. Accordingly, more time for grain growth of the DRX grain is given during the hot rolling at 1000 °C, causing the increase in the mean grain size of the HR1000. Meanwhile, the CR-A810 has the smallest average grain size of 5.5 ± 2.6 μm. Notably, each of the HRs shows a much wider grain size distribution from submicrons to tens of micrometers compared to the CR-A810 in Fig. S2 because the onset of the DRX is different for each grain in the HRs. It means that the time given for the grain growth during the hot rolling is different for each grain. In short, the sequential operation of the DRX during several hot rolling passes leads to uneven distribution of grain sizes: recently recrystallized grains are smaller than the early recrystallized ones, which is confirmed in the following ECC images.

The orientation distribution function (ODF) maps of the HRs in Fig. 1(a–c) show {111}//ND γ-fiber in common where $\varphi_2 = 45°$ and $\Phi = 55°$, which is a general rolling texture in FCC alloys. The retention of the rolling texture with low intensity of 2.4 to 3.5 originates from no preferred orientation during DRX. This is a typical feature of FCC metallic materials with low stacking fault energy (SFE), e.g., equiatomic CoCrFeMnNi [27] and twinning-induced plasticity steel [28]. Among the HRs, the HR800 exhibits the strongest γ-fiber because of the heavily deformed unrecrystallized coarse grains compared to the DRX grains. In contrast, no rolling texture is seen in the CR-A810 because static recrystallization (SRX) occurs by annealing. Instead, {001}<100> cube texture emerges in Fig. 1(d) due to the formation of annealing twins in the CR-A810 (Fig. S3), which is consistent with that reported for other metallic materials with low SFE [27]. The cube texture weakens the rolling textures during the annealing process accompanying the SRX [29].

Details of the DRX grains in the as-hot-rolled HR900 are probed by ECC imaging in Fig. 2. Given the fully DRXed microstructure of the HR900 in Fig. 1(b), the next round of DRX at the grain boundary of a preexisting DRX grain forms a necklace structure in Fig. 2(a). Note that the grain boundary is a preferential nucle-

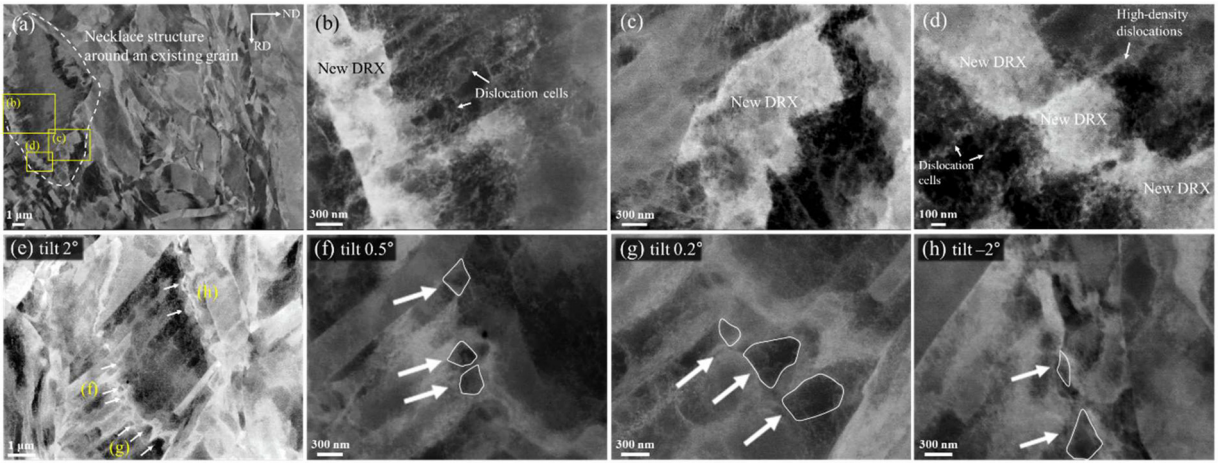

Fig. 2. ECC images of the initial HR900 with different grain sizes of the DRX grains. (a, e) New DRX grains on the grain boundaries of a preexisting DRX grain. (b–d) Magnified views of the new DRX grains in (a) with a tilt angle of 2°. (f–h) Submicron-scale DRX grains indicated by white arrows around a coarse DRX grain in (e) with various ECCI tilt angles: (e) 2°, (f) 0.5°, (g) 0.2°, and (h) −2°.

ation site for DRX [30]. In the magnified views in Fig. 2(b–d), the newly DRXed submicron-scale grains are much finer than the adjacent coarse DRX grains. The coarse DRX grain exhibits dislocation cells generated by the hot rolling in Fig. 2(b, d). By modulating the ECCI tilt angles at a different site with an analogous morphology of DRX grains in Fig. 2(e–h), relatively fine DRX grains around a coarse DRX grain exhibit clear dark images indicated by white arrows in Fig. 2(f–h) while dislocation cells are observed in the dark and coarse DRX grain in Fig. 2(e). That is, the new DRX grains have lower dislocation density than the preexisting DRX grain. This conforms to the dislocation consuming effect of DRX by the nucleation of new grains involving grain boundary migration [30]. Because the grain boundary migration is a thermally activated process [31], higher rolling temperature is beneficial to more active DRX: the DRX occurs on multiple occasions during the several hot rolling passes. In brief, the different onset of the DRX gives microstructural heterogeneity of not only the wide distribution of grain size but also the internal dislocation density among the grains in the HRs.

Based on the different dislocation densities among the DRX grains, the grain boundaries distinguish the microstructural heterogeneity consisting of the soft and hard grains. By the tensile deformation, the strain incompatibility between the soft and hard grains causes the dislocation pile-ups, developing the HDI back stress at the grain boundary into the recently DRXed soft grain [32,33]. Among the HRs, the HR900 has the largest fraction of grain boundaries because of the smallest average grain size. As a result, the average GND density of the HR900 exhibits the highest value among the HRs in Fig. S4(a) from the EBSD scans in Fig. 1. In contrast, the total dislocation density increases as the hot rolling temperature decreases as shown in Fig. S4(c) based on the CMWP method from the XRD profiles in Fig. S4(b). It is attributed that the GND density related to the microstructural heterogeneity is not always proportional to statistically stored dislocation density, which is associated with the amount of rolling deformation [34]. Indeed, the total dislocation density is the highest in the HR800 while the GND density by the microstructural heterogeneity is the highest in the HR900 as shown in Fig. S4(a, c).

3.2. Tensile properties at −196 °C

On the uniaxial tensile properties at −196 °C, the as-hot-rolled HRs have higher yield strength than the cold-rolled and annealed ones in Fig. 3(a): 659 ± 1, 770 ± 9, 744 ± 11, and 523 ± 20 MPa for the HR800, HR900, HR1000, and CR-A810, respectively. To verify the effect of the microstructural heterogeneity of the HRs on the back stress during the cryogenic tensile tests, loading-unloading-reloading (LUR) tests were conducted for the HR900 and the CR-A810. With unloading (σ_u) and reloading (σ_r) yield stresses of each LUR loop in Fig. S5(a), the back stress (σ_b) can be calculated as follows [33]:

$$\sigma_b = \frac{\sigma_u + \sigma_r}{2} \quad (1)$$

In Fig. 3(b), the HR900 has higher HDI back stress than the CR-A810 during the tensile deformation. It can be attributed to the microstructural heterogeneity in the hot-rolled MEAs, as elucidated in Figs. 1 and 2. The microstructural evidence for the back stress hardening is in the following tensile deformed microstructures.

The emphasis of the tensile properties is on two points: one is the superior uniform elongation of ~45% of the HRs despite the as-rolled states, and the other is the higher yield strength of the HR900 than that of the HR800 though the total dislocation density is higher in the HR800. The strain hardening behavior by the DIMT influencing the uniform elongation is nearly identical for all the samples, see Fig. 3(c). The noticeable difference between the HRs and the CR-A810 is that the HRs exhibit yield point phenomena (YPP) and the resulting Lüders elongation in Fig. 3(a, d), which will be further interpreted with deformed microstructures in Section 3.4. To access the rationale behind the lower yield strength of the HR800 than that of the HR900 in Fig. 3(d), the initial and tensile deformed microstructures of the partially DRXed HR800 are demonstrated below.

3.3. Microstructural evolution of the hot-rolled MEAs by tensile deformation

In the initial state of the HR800, a number of band-like substructures elongated along the RD exist in an unrecrystallized grain in Figs. 4(b) and S6. In the corresponding unrecrystallized grain, an EBSD phase map (Fig. 4(c)) and a misorientation profile (Fig. 4(f)) along the white arrows in Fig. 4(d, e) clarify the absence of BCC phase exhibiting high-angle misorientations. It should be noted that the misorientation angles of 1°–2° in Fig. 4(f) conform to those of microband boundaries [35]. The formation of the microbands arises from the rotation of misoriented domains by hot rolling (especially in unrecrystallized grains), thus the microbands are bounded by GNDs [36]. In Fig. 4(f), the peaks of kernel average misorientation (KAM) value associated with the GND density

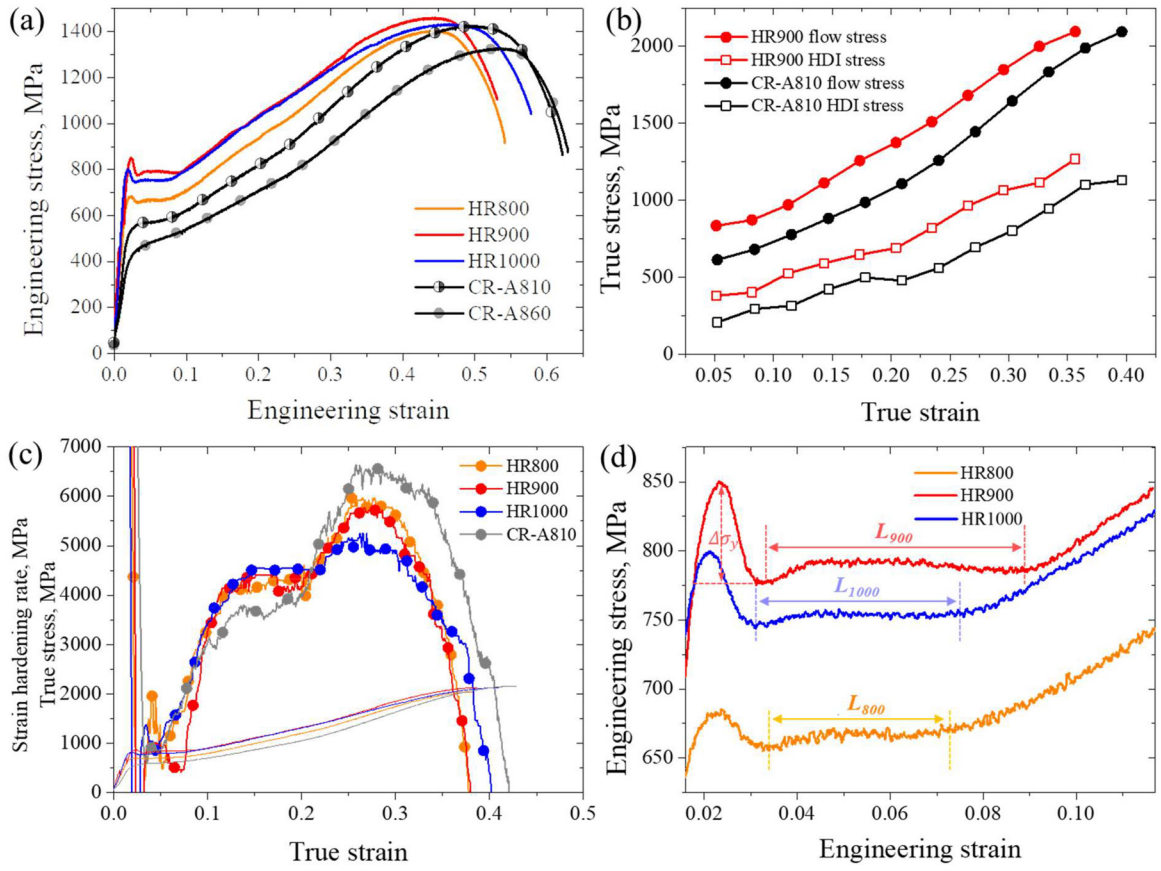

Fig. 3. Tensile properties at −196 °C of the MEAs after different thermo-mechanical control processes. (a) Engineering stress-strain curves with a nominal strain rate of 10^{-3} s^{-1}. (b) Flow and HDI back stresses of HR900 and CR-A810 according to the LUR tests. For the LUR loops, please refer to Fig. S5(a). (c) Strain hardening rate and true stress-strain curves. (d) Enlarged engineering stress-strain curves of the HRs exhibiting different Lüders elongation after yield point phenomena.

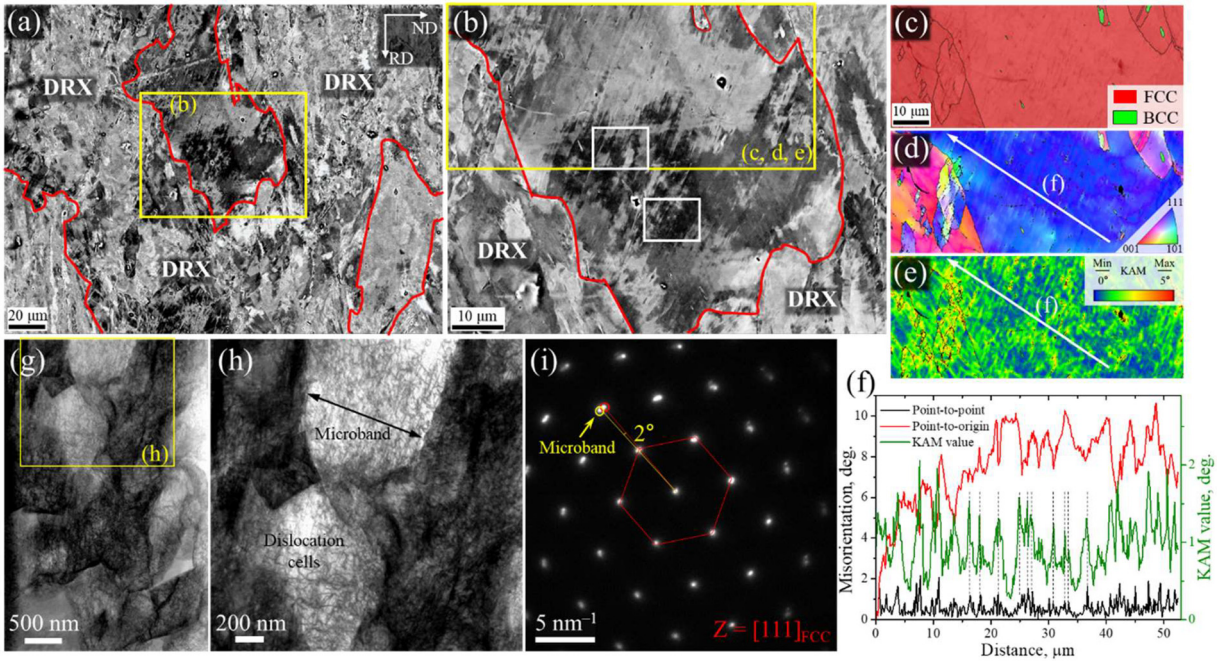

Fig. 4. Initial microstructures of the partially DRXed HR800. (a, b) ECC images where (b) is an enlarged part of an unrecrystallized coarse grain in (a). EBSD (c) phase map, (d) IPF map, and (e) KAM map with a step size of 0.1 μm according to a yellow box in (b). The enlarged ECC images for white boxes in (b) are given in Fig. S6. (f) A misorientation profile juxtaposed with KAM values in a green line along the white arrows in (d, e). (g, h) Bright-field STEM micrographs where (h) is framed in (g). (i) An SAD pattern corresponding to (h).

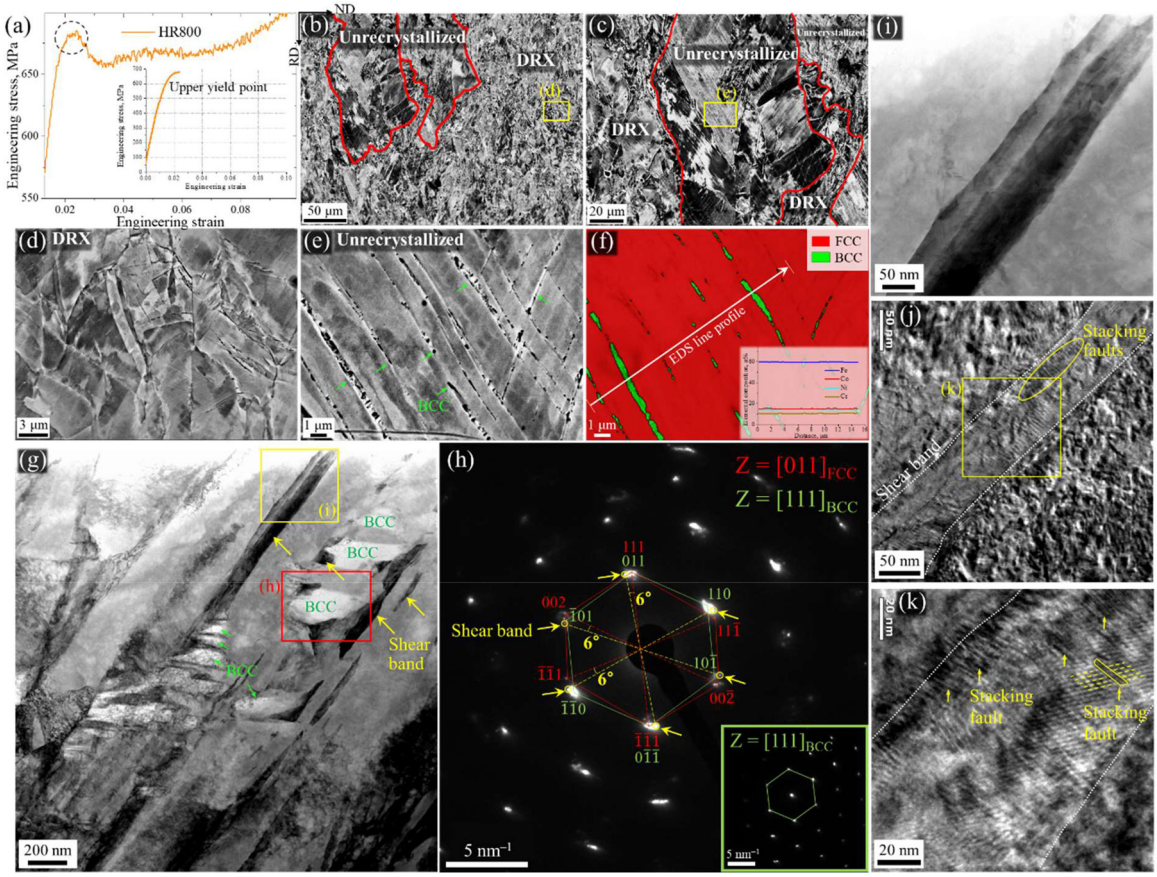

Fig. 5. Microstructures of the HR800 after the tensile deformation by upper yield point. (a) An engineering stress-strain curve by the applied stress reaching (inset of (a)) upper yield stress. (b–e) ECC images tilted by 2° and (f) an EBSD phase map with a step size of 40 nm corresponding to (e). (d) DRX and (e) unrecrystallized grains are framed in (b, c), respectively. One-dimensional EDS line profile in the inset of (f) along a white arrow in (f). (g) A bright-field STEM image of an unrecrystallized grain and (h) an SAD pattern for a red box in (g). The inset of (h) is only for the BCC grain in the red box. Bright-field (i) STEM and (j, k) TEM images for a shear band in a yellow box in (g), where (k) is framed in (j).

are coincident with the misorientation peaks. That is, the boundaries with misorientation angles of 1°–2° have relatively high GND density, supporting the existence of microbands. Within the microbands, numerous dislocation cells are observed in Fig. S6(b, c) as well as the bright-field scanning TEM (STEM) images in Fig. 4(g, h). The selected area diffraction (SAD) pattern in Fig. 4(i) corresponding to the area of Fig. 4(h) shows a deviation of ~2° from the FCC spot due to the hot rolling-induced microbands, in line with the misorientation profile in Fig. 4(f). Such deviations in the diffraction pattern have been reported to be attributed to the formation of microbands [37].

To clarify the microstructural evolution prior to the yielding of the HR800, an interrupted tensile test at −196 °C by the upper yield point was conducted, see Fig. 5(a). The unrecrystallized grain with a large amount of rolling deformation has profuse shear bands in Fig. 5(e), in contrast to the DRX grains in Fig. 5(d). More importantly, BCC phase is observed along the shear bands in an unrecrystallized grain by ECCI in Fig. 5(e) and EBSD phase map in Fig. 5(f) though the tensile stress only reached the upper yield stress. A bright-field STEM image in Fig. 5(g) of an unrecrystallized grain assures the generation of the BCC phase along the shear bands. The SAD pattern in Fig. 5(h) for a red box in Fig. 5(g) reveals the Kurdjumov-Sachs orientation relationship between the FCC and BCC phase [38], confirming the formation of martensite. Moreover, additional spots deviating by ~6° from the diffraction pattern of the FCC phase are observed. Given that shear bands have been reported to exhibit misorientations of 6°–12° [39], the SAD pattern in Fig. 5(g) illustrates the presence of BCC martensite along the shear bands. No deformation twin bundles are observed in Fig. 5(i); instead, stacking faults are identified in the nano-scale shear band in bright-field TEM images in Fig. 5(j, k), which are distinct from the microbands in Fig. 4(h). It should be noted that the deviation angle of the shear bands is higher than that of the microband, which is ~2° in Fig. 4(i). It can be inferred that the tensile deformation has increased the misorientation angles of the dislocation substructures because the microband involves the formation of narrow shear zones surrounded by dislocations [40]. In short, the microbands with profuse dislocation cells in the unrecrystallized grains in the HR800 contribute to the generation of shear bands, which are beneficial to provoking martensitic transformation. Considering that the martensitic transformation occurred during the elastic deformation at −196 °C without plastic strain, the BCC phase is stress-induced martensite. By an EDS line profile along a white arrow in Fig. 5(f), the elemental compositions for the FCC and BCC phase are the same in the inset of Fig. 5(f), indicating that the martensitic transformation does not involve a diffusion-controlled process.

Once the tensile deformation further proceeds by the lower yield point in Fig. 6(a), the BCC martensite is observed along the shear bands in a coarse unrecrystallized grain in Fig. 6(c), similar to Fig. 5(e). The ECC images of Fig. 6(b, c) are tilted by −2°. With a different tilt angle of 2°, planar arrays of dislocations in a DRX grain which are piled up at the grain boundary between the DRX and unrecrystallized grains are clearly observed in Fig. 6(d). Note that the interval between the dislocation pile-ups marked by white arrows is relatively narrow near the grain boundary, which is

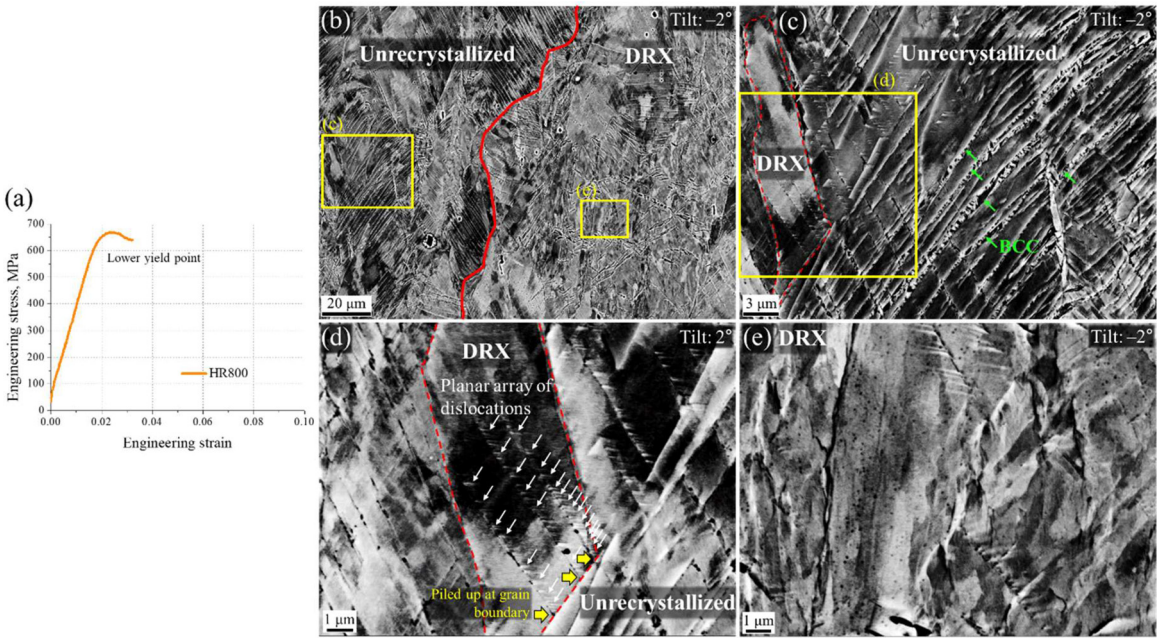

Fig. 6. Microstructures of the HR800 after the tensile deformation by lower yield point. (a) An engineering stress-strain curve by the applied stress reaching lower yield stress. (b–e) ECC images of deformed microstructures by the lower yield point with tilt angles of (b, c, e) –2° and (d) 2°. (d) Planar arrays of dislocations piled up at the grain boundary into a relatively soft DRX grain.

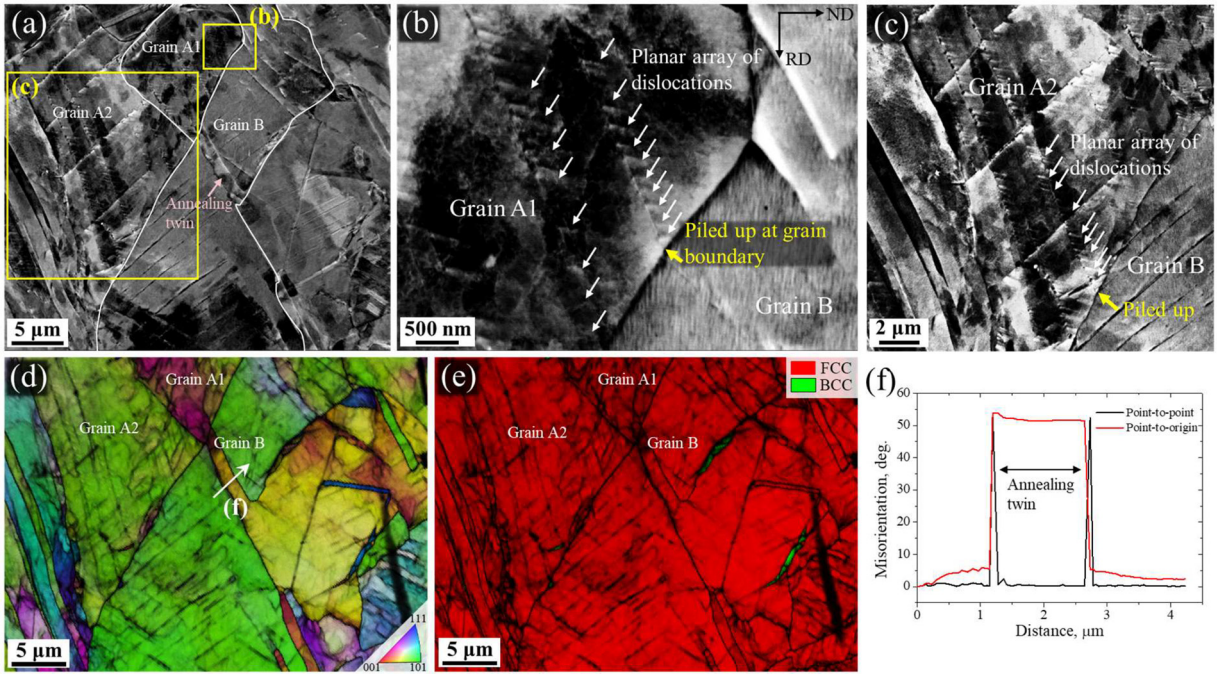

Fig. 7. Tensile deformed microstructures of the HR1000 by ε of 0.03. Enlarging the ECC image of the HR1000 (a), planar arrays of dislocations piled up at grain boundaries between the grains (b) A1 and B and (c) A2 and B are exhibited. EBSD (d) IPF and (e) phase maps of (a) with a step size of 60 nm. (f) A misorientation profile along a white arrow in (d).

a feature of the dislocation pile-ups. Indeed, the DRX grain where the planar arrays of the dislocations are piled up is softer than the unrecrystallized grain. Meanwhile, the lack of martensite in the DRX grains in Fig. 6(e) ensures that the stress-induced martensitic transformation preferentially occurs in the coarse unrecrystallized grains before the tensile yielding of the HR800.

Between the DRX grains, the dislocation pile-ups are also confirmed after yielding. Fig. 7 gives ECC images of the HR1000 deformed by engineering strain (ε) of 0.03. Grain B is coarser than grains A1 and A2 in Fig. 7(a) and all the grains are DRXed as revealed in Fig. 1(c). Despite the low tensile strain, planar arrays of dislocations in the relatively fine grains – grain A1 in Fig. 7(b) and A2 in Fig. 7(c) – are piled up at grain boundaries between the grains A1 or A2 and B. As observed in Fig. 6(d), the distance between each piled-up dislocation is closer in the vicinity of the grain boundary as indicated by white arrows in Fig. 7(b, c). Therefore, it can be deduced that the HDI strengthening of the as-hot-rolled MEA in Fig. 3(b) is promoted by the uneven distribution of

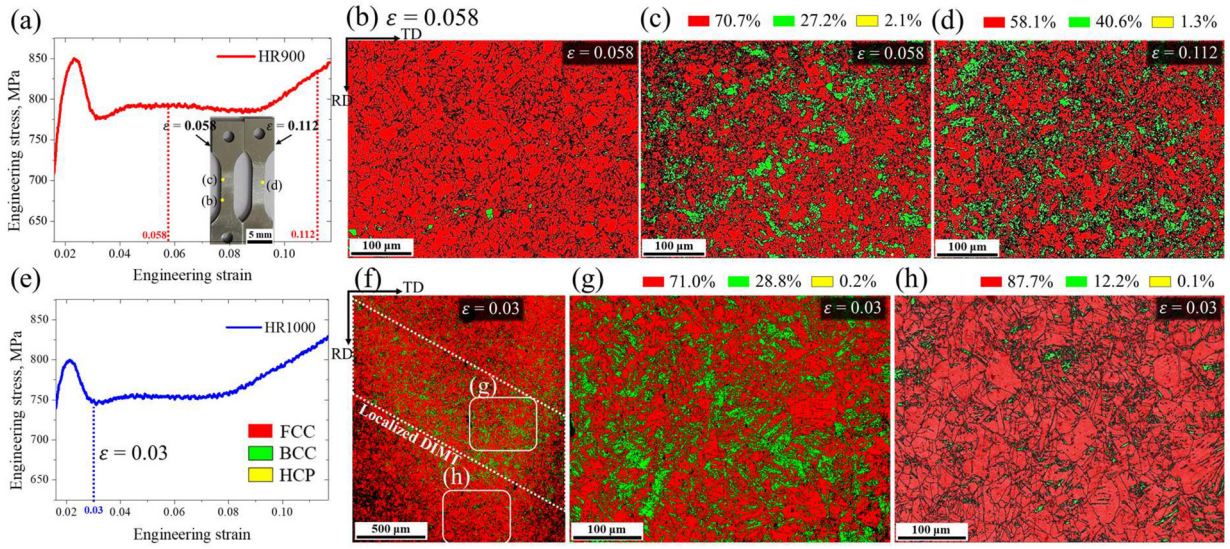

Fig. 8. Deformed microstructures of the HR900 and HR1000 after the onset of Lüders band. Stress-strain curves of the (a) HR900 and (e) HR1000. An OM image in an inset of (a) shows tensile specimens of the HR900 after the ε of 0.058 and 0.112. EBSD phase maps of the HR900: (b) outer and (c) inner areas of the Lüders band when ε reaches 0.058 and (d) when ε reaches 0.112. For the EBSD phase maps of the HR1000, (f) shows when ε reaches 0.03 and magnified regions of the (g) inner and (h) outer parts of the Lüders band in (f) are shown aside.

grain size and internal dislocation density in Fig. 2 during the tensile deformation at −196 °C. According to the EBSD phase map in Fig. 7(e) corresponding to Fig. 7(a), the grains A1, A2, and B are FCC grains. The misorientation profile in Fig. 7(f) along the white arrow in the IPF map in Fig. 7(d) exhibits an annealing twin in the grain B, indicating that the grain B is a DRX grain. It concurs with the fully DRXed microstructure of the HR1000 in Fig. 1(c).

3.4. Lüders band propagation

The tensile specimens of the HR900 after the interrupted tensile tests at −196 °C by ε of 0.058 and 0.112 after the YPP are shown in an optical microscopy (OM) image in an inset of Fig. 8(a). The former is during the propagation of the Lüders band and the latter is after the end of the propagation. During the Lüders elongation, the stress-concentrated Lüders band is prone to generate the stress-induced BCC martensite as shown in Fig. 8(c) compared to the outer region of the Lüders band in Fig. 8(b). The BCC martensite of an areal fraction of 27.2% was generated in the Lüders band by ε of 0.058. As the tensile deformation further proceeds by ε of 0.112, the Lüders band has been fully propagated along the gage section in Fig. 8(a), and the HR900 is uniformly deformed with an increased BCC fraction of 40.6% in Fig. 8(d).

Similar to the case of the HR900, for the deformed HR1000 by ε of 0.03 at the onset of Lüders elongation in Fig. 8(e), a localized DIMT, i.e., the Lüders band has occurred in a broad view in Fig. 8(f). In the Lüders band, the BCC martensite has been generated by stress-induced martensitic transformation in Fig. 8(g), given that the front of the Lüders band is a stress-concentrated region [41]. The areal fraction of the BCC martensite in the Lüders band of the HR1000 by ε of 0.03 (28.8%) is comparable to that in the Lüders band of the HR900 by higher ε of 0.058 (27.2%) in Fig. 8(c). In other words, the HR1000 exhibits faster DIMT kinetics during the propagation of the Lüders band than the HR900. As in the HR900, the outer area of the Lüders band in the HR1000 has a small amount of BCC martensite in Fig. 8(h).

After the end of nonuniform deformation by the Lüders band propagation, an increase in the fraction of the deformation-induced BCC martensite is uniformly observed in the gage section of the deformed HR1000 by ε of 0.1 in Fig. 9(a). In an ECC image of the same sample in Fig. 9(b), plate-type BCC martensite with a distinctly different morphology from the FCC matrix has emerged, indicating the stress-induced martensite [42]. The uniform TRIP behavior all over the gage section after the end of Lüders elongation of the HRs is enough to bias the strain hardening rate upward as shown in Fig. 3(c).

4. Discussion

4.1. Softening by martensitic transformation during elastic deformation

During the elastic deformation by the tensile test, stress-induced BCC martensite is formed in unrecrystallized coarse grains in HR800 in Figs. 5(e) and 6(c), compared to the fully DRXed HR900 and HR1000. The unrecrystallized grains possess profuse dislocations and shear bands by a large amount of rolling deformation, which stimulates the stress-induced BCC martensitic transformation. In TRIP steels, martensite has a higher specific volume than austenite [43]. Thus, the phase transformation from the austenite to the martensite induces strain relaxation and transformation of the stress state from tension to compression [44]. The softening effect of the TRIP behavior has been reported in different kinds of TRIP-assisted materials for decades: TRIP steels [43] and MPEAs [44]. Similarly, in our previous study, the stress state from tension to compression was verified by a neutron diffraction analysis [45]. It is intriguing that as temperature decreases below M_s temperature for the TRIP steel, the tensile yield stress exhibits a noticeable degradation due to the formation of athermal martensite [43]. Thereby, it can be confidently argued that the martensitic transformation during the elastic deformation is responsible for the lower yield strength of the partially DRXed HR800 than those of the fully DRXed HR900 and HR1000.

4.2. Strengthening contributors of the hot-rolled MEAs

The yield stress (σ_y) of the MEA after each thermo-mechanical process can be estimated as follows:

$$\sigma_y = \sigma_0 + \sigma_{ss} + \sigma_\rho + \sigma_{gb} + \sigma_{HDI} \quad (2)$$

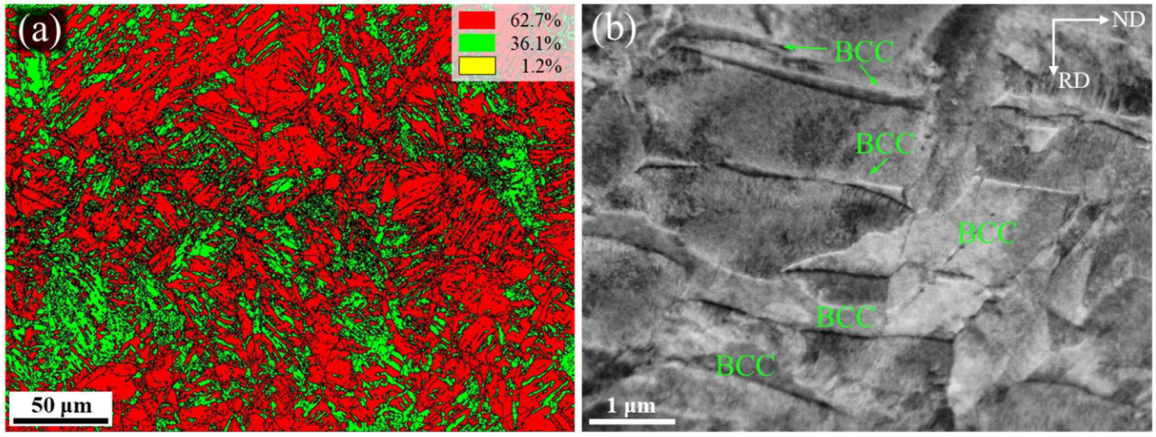

Fig. 9. Tensile deformed microstructures of the HR1000 by ε of 0.1. (a) An EBSD phase map with a step size of 0.3 μm and (b) an ECC image. Red, green, and yellow interpret the FCC, BCC, and HCP phases, respectively.

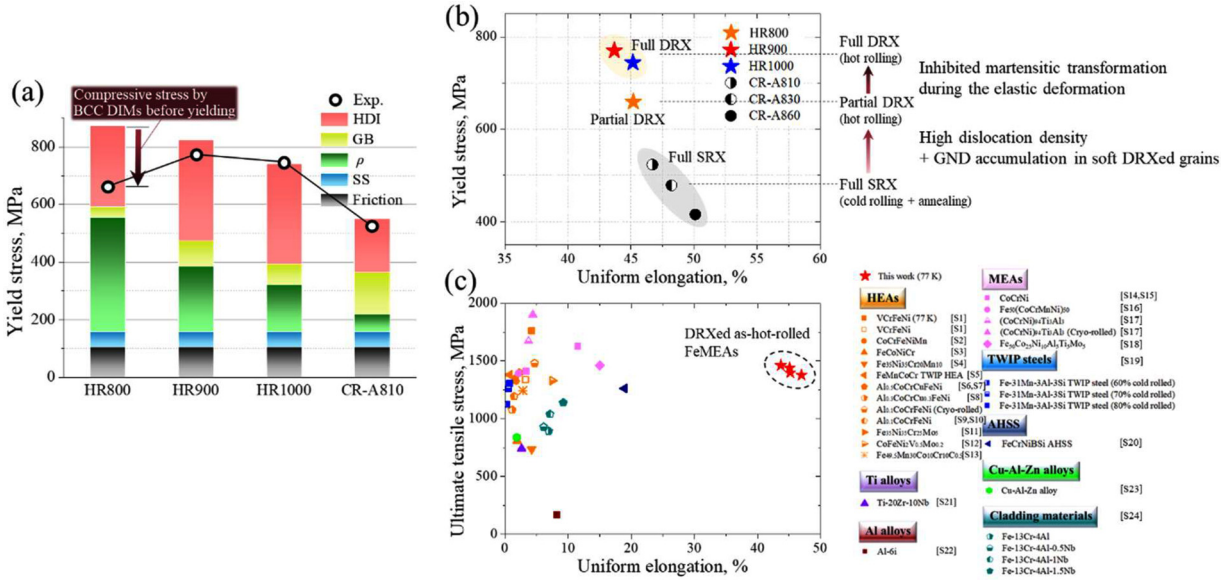

Fig. 10. Strengthening mechanisms and the corresponding tensile properties. (a) Strengthening contributors of yield stresses of the HRs and the CR-A810 plotted with the experimental yield stresses. (b) Tensile properties at −196 °C of the MEAs assorted by the grain characteristics according to different thermo-mechanical processes. (c) Ashby plot of tensile properties for a variety of as-rolled metallic materials. The references used in (c) are given in Supplementary Information.

where σ_0 is friction stress (103 MPa for the present MEA [46]), σ_{ss} is solid solution strengthening, σ_ρ is dislocation strengthening, σ_{gb} is grain boundary strengthening, and σ_{HDI} is hetero-deformation-induced strengthening. The effect of texture on the yield stress is neglected regarding the low intensity of the hot-rolled textures in Fig. 1.

The solid solution strengthening for the present FCC-based MEA is estimated to be 53.7 MPa based on Fleischer's substitutional hardening model [47–49]. For the details of the model, readers are referred to Appendix A. For the σ_ρ derived from the interactions among forest dislocations by the Taylor equation, $\sigma_\rho = M\alpha Gb\rho^{1/2}$, the dislocation density (ρ) from the CMWP fitting in Fig. S4(c) is used. The parameters M, α, G, and b are the Taylor factor (3.09 for FCC [13]), a constant (0.2 [46]), a shear modulus (82.3 GPa for the MEA [50]), and the magnitude of the Burgers vector (0.253 nm [46]), respectively. The Hall-Petch relationship accounts for the σ_{gb}: $\sigma_{gb} = kd^{-1/2}$ (k: 339 MPa $m^{1/2}$ [46] and d: mean grain size in Fig. S2). The intergranular long-range HDI strengthening of the HRs is confirmed by the discrepancies of the back stresses at the yield point between the heterogeneous HRs and the homogeneous CR-A810, determined by the LUR tests in Fig. S5.

Fig. 10(a) compiles the strengthening contributors of the HRs and CR-A810. Bar graphs represent theoretical yield stresses with each strengthening mechanism and the experimental values are plotted in a line graph. Note that only the calculated yield stress of the HR800 has a large mismatch of ~200 MPa with the experimental yield stress. It is attributed to the softening effect of the volume expansion by the stress-induced martensitic transformation prior to yielding, which was not examined in the yield stress contributors in Eq. (2).

The yield stress increases in the order of the following classified groups according to the grain characteristics in Fig. 10(b): full SRX (cold-rolled and annealed ones), partial DRX (HR800), and full DRX (HR900 and HR1000) without a significant reduction in uniform elongation. Compared to the SRX group, both the high dislocation density of the as-hot-rolled states and the additional dislocation accumulation in the relatively soft and fine DRX grains lead to the higher yield stress of the DRX groups. Between the DRX groups, full DRX exhibits higher yield stress than partial DRX because of the martensitic transformation prior to yielding in the partially DRXed HR800. Here comes another beneficial effect of the full DRX on the yield stress apart from the HDI strengthening due

to the wide distribution of the DRXed grain sizes: inhibiting the martensitic transformation before yielding.

Fig. 10(c) exhibits combinations of uniform elongation and ultimate tensile stress for a variety of as-rolled metallic materials. To the best of our knowledge, the present DRXed metastable MEAs exhibit record-breaking uniform elongation of ~45% among the as-rolled states. It is attributed to the effect of microstructural heterogeneity of the wide distribution of grain sizes on strain hardening as well as the TRIP effect. The strengthening effect of the back stress in the relatively soft DRX grains is obvious by pile-ups of planar array of dislocations in Fig. 7(b, c). Meanwhile, the directional back stress offsets effective resolved shear stress for dislocation slip [32]; the soft grain sustains higher plastic strain by the promoted dislocation slip. Consequently, the microstructural heterogeneity from the different onset of the DRX produces extra strain hardening, called HDI strain hardening apart from the TRIP effect.

4.3. Yield point phenomenon and Lüders elongation

The deformation behavior right after the yield point of the hot-rolled MEAs accompanying the YPP is important because the as-rolled materials mostly exhibit catastrophic uniform elongation soon after the yielding in Fig. 10(c) due to the insufficient strain hardening capacity. As described in Section 4.1, external stress can be relieved by a larger specific volume of BCC martensite than that of the FCC phase through martensitic transformation. Moreover, the martensitic transformation generates mobile dislocations in neighboring FCC grains [51]. According to Eqs. (3) and (4), a rapid increase in mobile dislocation density causes a sudden decrease in the applied stress, viz., a yield drop [41,52]:

$$\dot{\gamma}^{\mathrm{p}} = b\rho_{\mathrm{m}}\left(\frac{\tau_{\mathrm{eff}}}{D_{\tau}}\right)^{n_0} \tag{3}$$

$$\tau_{\mathrm{eff}} = (\tau - \tau_{\mathrm{c}}) \tag{4}$$

where $\dot{\gamma}^{\mathrm{p}}$ is plastic shear strain rate, b is the magnitude of the Burgers vector, ρ_{m} is density of mobile dislocations, and τ_{eff} is effective shear stress, i.e., excess shear stress over the interaction stress τ_{c} in Eq. (4) with Macaulay brackets. The parameter n_0 is stress-sensitivity exponent and D_{τ} is shear drag stress [41].

Note that the stress-induced martensitic transformation is activated by a sufficient stress level once the yield point is reached in the fully DRXed HR900 and HR1000, as shown in Fig. 8(c, g), respectively. Hence, the yield drop in the as-rolled HR stems from the initiation of the martensitic transformation from FCC to BCC phase at the yield point due to stress concentration. In sharp contrast, for the annealed CR-A810, most of the dislocations generated during cold rolling are dissipated by annealing as seen in Fig. S4(c). In this regard, the CR-A810 has much lower yield strength than HR: stress-induced martensitic transformation is deemed difficult to occur by the yield point. Moreover, the lack of {111}//ND γ-fiber in CR-A810 compared to HR in Fig. 1 makes it less prone to awaken DIMT because shear favorably occurs along close-packed {111} planes of FCC grains, leading to the phase transformation to {110} BCC grains [53].

Among the HRs, HR800 exhibits the lowest amount of yield drop in Fig. 3(d). Note that the martensitic transformation occurs in unrecrystallized grains prior to yielding in the HR800 in Fig. 5(e), resulting in a decrease in flow stress. The martensitic transformation before the onset of yielding reduces the upper yield stress of HR800, thus attenuating the YPP in HR800. On the contrary, the onset of DIMT at the upper yield point leads to a more significant decrease in flow stress for the fully DRXed HR900 and HR1000. The noticeable amount of martensite (28.8%) in the Lüders band in HR1000 deformed by an engineering strain of only 0.03 in Fig. 8(g) supports that the DIMT has a significant impact on the YPP.

The YPP accompanies the onset of the Lüders band where the stress is locally concentrated in the hot-rolled MEAs. In the metastable HRs, the stress concentration in the vicinity of the front of the Lüders band provokes the DIMT, which generates mobile dislocations [51]. Because the mobile dislocations are beneficial to the propagation of the Lüders band [51], the local DIMT promotes a higher velocity of the band propagation. Meanwhile, the HR1000 exhibits faster DIMT than the HR900 in Fig. 8(c, g). It is attributed to the larger mean grain size of the HR1000 than that of the HR900 because elastic strain energy increases with a decrease in the average grain size of FCC grains, which decreases the ability to nucleate martensite and improves the average stability of the FCC grains [54]. Moreover, interfacial back stresses at the FCC grain boundaries hinder the growth of the BCC nuclei [55]. Therefore, the Lüders band in the HR1000 with the higher DIMT kinetics propagates faster than that in the HR900; the Lüders elongation, from the beginning to the completion of the DIMT in the whole gage section, is lower in the HR1000 in Fig. 3(d). The DIMT in the HR800 including unrecrystallized grains is deemed to be the most active, thus the Lüders elongation of the HR800 is the lowest among the HRs in Fig. 3(d). In brief, the stress-induced martensitic transformation in the HRs prevents early necking by triggering the propagation of the Lüders band with the aid of mobile dislocations. Thanks to the DIMT apart from the effect of the uneven distribution of the DRX grain characteristics on the HDI strain hardening, the hot-rolled MEAs result in the unprecedented uniform elongation of ~45% by the desirable strain hardening capacity.

4.4. Simplification of thermo-mechanical processes and future works

Another merit of this paper is to introduce the hot rolling without further annealing process. The simplified thermo-mechanical processes can offer considerable industrial profits. Compared to the effect of annealing temperature and time on the recrystallized microstructures [56–59], DRX in high-entropy alloys through hot rolling has not received as much attention. However, based on the generally accepted fact that the DRX kinetics is closely related to temperature and strain rate, the control of hot rolling temperature and thickness reduction ratio would decisively affect the DRX microstructures. In other words, an increase in temperature and a decrease in strain rate lead to a decrease in Zener-Hollomon parameter and promote the driving force for DRX [30]. Thus, controlling the hot rolling parameters properly so that DRX occurs in multiple rounds and a wide distribution of grain size appears is a salient key to rendering the microstructural heterogeneity. In this wise, it can be confidently argued that the DRX-induced heterostructuring is not limited to the FeMEAs but can be applied to a variety of metallic materials. Further works to apply the DRX-induced heterostructuring strategy to other metallic materials, e.g., dual-phase steels and other MPEAs with simplified thermo-mechanical histories, are highly encouraged. Further, once a substantial amount of microstructural features with different hot rolling conditions are gathered, it will be easier to predict the DRX microstructures.

5. Conclusions

The current study introduces uneven distribution of the grain sizes and internal dislocation densities of the as-hot-rolled FeMEAs with enhanced mechanical properties at liquid nitrogen temperature. The salient strengths of this research through the present thermo-mechanical processes are demonstrated below.

(1) Hot rolling of the present MEA triggers DRX on the grain boundary of the preexisting grain, forming a necklace structure. The successive operation of the DRX by several hot rolling

passes leads to the heterogeneity of grain characteristics comprising the grain size and internal dislocation density.

(2) The hot-rolled MEAs exhibit desirable uniform elongation of ~45% at −196 °C comparable to the conventionally fabricated ones by cold rolling and annealing. The effect of HDI strain hardening as well as stress-induced martensitic transformation results in remarkable uniform elongation despite the as-rolled states. Moreover, high dislocation density and HDI strengthening contribute to the enhanced yield strength of the as-hot-rolled MEAs compared to that of the cold-rolled and annealed ones.

(3) When the hot rolling temperature decreases from 1000 °C to 900 °C, a decrease in mean grain size and an increase in dislocation density induce higher grain boundary strengthening and dislocation strengthening, respectively. In contrast, as the rolling temperature further decreases from 900 °C to 800 °C, the grains are partially recrystallized. During the tensile test at −196 °C, the stress-induced BCC martensitic transformation in unrecrystallized grains prior to yielding attenuates the yield stress of the partially DRXed MEA.

(4) The stress localization after yield drop in the HRs induces local DIMT generating mobile dislocations, which facilitates the propagation of Lüders band and prevents early necking. The current findings demonstrate that the hot rolling-induced heterostructuring of grain characteristics without further annealing is a promising pathway to simplify the processing routes with better performance and industrial benefits.

Declaration of Competing Interest

The authors declare that they have no known competing financial interests or personal relationships that could have appeared to influence the work reported in this paper.

Acknowledgments

This work was financially supported by POSCO (No. 2021Y037), the Nano & Material Technology Development Program through the National Research Foundation of Korea (NRF) funded by Ministry of Science and ICT (No. RS-2023-00281246), and the National Research Foundation of Korea (NRF) grant funded by the Korea government (MSIP) (Nos. NRF–2021R1A2C3006662 and NRF-2022R1F1A1073796). J.L. acknowledges support from the Basic Science Research Program through the National Research Foundation of Korea (NRF) funded by the Ministry of Education (No. RS-2023-00276120).

Supplementary materials

Supplementary material associated with this article can be found, in the online version, at doi:10.1016/j.jmst.2023.09.007.

Appendix A

Fleischer's model can reveal the solid solution strengthening of FCC metallic materials according to the following formulae [26,47,48]:

$$\sigma_{ss} = \sum_i \left(\beta_i^2 x_i\right)^{\frac{1}{2}} \tag{A1}$$

$$\beta_i = \kappa G\left(\eta_i' + 16\delta_i\right)^{\frac{3}{2}} \tag{A2}$$

$$\eta_i' = \frac{\eta_i}{1 + 0.5\eta_i} \tag{A3}$$

$$\delta_i = \frac{|r_i - r_{Fe}|}{r_i} \tag{A4}$$

where β_i is a solid solution parameter, x_i is mole fraction, r_i is atomic radius of element i, G is the shear modulus of the MEA of 82.3 GPa [50], and κ is a fitting parameter of 0.0045 [48]. The two parameters $\eta_i = \frac{|G_i - G_{Fe}|}{G_{Fe}}$ and δ_i are the shear modulus (G_i) and the lattice distortion of element i with respect to pure iron, respectively. The parameter values of each element are represented in Table A1.

Table A1
Values of parameters with respect to pure iron for Fleischer's model.

	G_i (GPa [49])	r_i (pm [26])	δ_i	x_i	η_i	β_i (MPa)
Fe	81.9	126	–	0.6	–	–
Co	82.1	125	0.007937	0.15	0.002442	17.244
Cr	90.0	128	0.015873	0.1	0.098901	76.098
Ni	78.5	124	0.015873	0.15	0.041514	59.231

References

[1] B. Gludovatz, A. Hohenwarter, D. Catoor, E.H. Chang, E.P. George, R.O. Ritchie, Science 345 (2014) 1153–1158.
[2] J. Yi, L. Yang, L. Wang, M. Xu, L. Liu, Met. Mater. Int. 28 (2022) 227–236.
[3] H. Wang, Z. Hu, J. Cao, S. Zhang, T. Cheng, Q. Wang, Met. Mater. Int. 28 (2022) 514–522.
[4] B. Cantor, I.T.H. Chang, P. Knight, A.J.B. Vincent, Mater. Sci. Eng. A 375-377 (2004) 213–218.
[5] G.T. Lee, J.W. Won, K.R. Lim, M. Kang, H.J. Kwon, Y.S. Na, Y.S. Choi, Met. Mater. Int. 27 (2021) 593–602.
[6] Y.H. Jo, K.Y. Doh, D.G. Kim, K. Lee, D.W. Kim, H. Sung, S.S. Sohn, D. Lee, H.S. Kim, B.J. Lee, S. Lee, J. Alloy. Compd. 809 (2019) 151864.
[7] H. Luo, Z. Li, A.M. Mingers, D. Raabe, Corros. Sci. 134 (2018) 131–139.
[8] S. Son, S. Kim, J. Kwak, G.H. Gu, D.S. Hwang, Y.T. Kim, H.S. Kim, Mater. Lett. 300 (2021) 130130.
[9] J. Chen, X. Zhou, W. Wang, B. Liu, Y. Lv, W. Yang, D. Xu, Y. Liu, J. Alloy. Compd. 760 (2018) 15–30.
[10] J.W. Bae, J.B. Seol, J. Moon, S.S. Sohn, M.J. Jang, H.Y. Um, B.J. Lee, H.S. Kim, Acta Mater. 161 (2018) 388–399.
[11] J.W. Bae, H.S. Kim, Scr. Mater. 186 (2020) 169–173.
[12] C. Ioannidou, A. Navarro-López, R.M. Dalgliesh, A. Rijkenberg, X. Zhang, B. Kooi, N. Geerlofs, C. Pappas, J. Sietsma, A.A. van Well, S.E. Offerman, Acta Mater. 220 (2021) 117317.
[13] J. Ren, Y. Zhang, D. Zhao, Y. Chen, S. Guan, Y. Liu, L. Liu, S. Peng, F. Kong, J.D. Poplawsky, G. Gao, T. Voisin, K. An, Y.M. Wang, K.Y. Xie, T. Zhu, W. Chen, Nature 608 (2022) 62–68.
[14] J. Moon, J.M. Park, J.W. Bae, H.S. Do, B.J. Lee, H.S. Kim, Acta Mater. 193 (2020) 71–82.
[15] O. Bouaziz, H.S. Kim, J. Lee, Y. Estrin, Met. Mater. Int. 29 (2023) 280–292.
[16] G.F. Liu, T.J. Chen, Met. Mater. Int. 28 (2022) 2919–2933.
[17] C. Han, Q. Fang, Y. Shi, S.B. Tor, C.K. Chua, K. Zhou, Adv. Mater. 32 (2020) 1903855.
[18] J. Lee, J.W. Bae, P. Asghari-Rad, H.S. Kim, Scr. Mater. 211 (2022) 114511.
[19] Y.H. Jo, S. Jung, W.M. Choi, S.S. Sohn, H.S. Kim, B.J. Lee, N.J. Kim, S. Lee, Nat. Commun. 8 (2017) 15719.
[20] J.W. Bae, J. Lee, A. Zargaran, H.S. Kim, Scr. Mater. 194 (2021) 113653.
[21] Y. Liu, R. Lai, C. He, K. Li, Y. Yang, W. Wu, Z. Fu, S. Xu, G. He, B. Gan, C. Huang, Mater. Charact. 186 (2022) 111795.
[22] M. Ebrahimian, M.S. Rizi, S.I. Hong, J.H. Kim, Sci. Technol. Adv. Mater. 24 (2023) 2186119.
[23] A. Javaid, F. Czerwinski, J. Magnes. Alloy. 7 (2019) 27–37.
[24] J. Lee, H. Park, S. Son, T. Nakano, H.S. Kim, J. Alloy. Compd. 965 (2023) 171469.
[25] S. Han, P. Eisenlohr, M.A. Crimp, Mater. Charact. 142 (2018) 504–514.
[26] H. Kwon, P. Sathiyamoorthi, M.K. Gangaraju, A. Zargaran, J. Wang, Y.U. Heo, S. Harjo, W. Gong, B.J. Lee, H.S. Kim, Acta Mater. 248 (2023) 118810.
[27] G.D. Sathiaraj, M.Z. Ahmed, P.P. Bhattacharjee, J. Alloy. Compd. 664 (2016) 109–119.
[28] L. Bracke, K. Verbeken, L.A.I. Kestens, Scr. Mater. 66 (2012) 1007–1011.
[29] B. Guo, R.K. Ray, S. Yoshida, Y. Bai, N. Tsuji, Scr. Mater. 215 (2022) 114706.
[30] S.M. Fatemi-Varzaneh, A. Zarei-Hanzaki, H. Beladi, Mater. Sci. Eng. A 456 (2007) 52–57.
[31] T. Sakai, A. Belyakov, R. Kaibyshev, H. Miura, J.J. Jonas, Prog. Mater. Sci. 60 (2014) 130–207.
[32] Y. Zhu, X. Wu, Prog. Mater. Sci. 131 (2023) 101019.
[33] M. Yang, Y. Pan, F. Yuan, Y. Zhu, X. Wu, Mater. Res. Lett. 4 (2016) 145–151.
[34] N. Wang, Y. Chen, G. Wu, Q. Zhao, Z. Zhang, L. Zhu, J. Luo, Mater. Sci. Eng. A 836 (2022) 142728.
[35] I. Gutierrez-Urrutia, A. Shibata, K. Tsuzaki, Acta Mater. 233 (2022) 117980.

[36] S. Zhang, Y. Liu, J. Wang, S. Qin, X. Wu, F. Yuan, Materials 15 (2022) 3542.
[37] J. Zhang, Z. Zhao, Q. Li, J. Luan, C.T. Liu, Y. Zhao, T. Yang, Adv. Powder Mater. 2 (2023) 100113.
[38] X. Geng, J. Gao, Y. Huang, S. Wang, Y. Zhang, G. Wu, H. Zhao, H. Wu, X. Mao, Acta Mater. 252 (2023) 118925.
[39] X. Li, S. Sun, Y. Zou, Q. Zhu, Y. Tian, J. Wang, Mater. Res. Lett. 10 (2022) 385–391.
[40] Y. Jia, C. Ren, S. Wu, Y. Mu, L. Xu, Y. Jia, W. Yan, J. Yi, G. Wang, J. Mater. Sci. Technol. 149 (2023) 73–87.
[41] F. Yoshida, Y. Kaneda, S. Yamamoto, Int. J. Plast. 24 (2008) 1792–1818.
[42] J. Yang, Y.H. Jo, W. An, H.S. Kim, B.J. Lee, S. Lee, H. Sung, S.S. Sohn, Acta Mater. 225 (2022) 117568.
[43] G.B. Olson, M. Cohen, Metall. Trans. A 13 (1982) 1907–1914.
[44] J. Li, Q. Fang, B. Liu, Y. Liu, Acta Mater. 147 (2018) 35–41.
[45] J.W. Bae, J. Jung, J.G. Kim, J.M. Park, S. Harjo, T. Kawasaki, W. Woo, H.S. Kim, Materialia 9 (2020) 100619.
[46] J.M. Park, P. Asghari-Rad, A. Zargaran, J.W. Bae, J. Moon, H. Kwon, J. Choe, S. Yang, J.H. Yu, H.S. Kim, Acta Mater. 221 (2021) 117426.
[47] R.L. Fleischer, Acta Metall. 11 (1963) 203–209.
[48] E.I. Galindo-Nava, P.E.J. Rivera-Díaz-del-Castillo, Acta Mater. 98 (2015) 81–93.
[49] T. Górecki, Mater. Sci. Eng. 43 (1980) 225–230.
[50] J.W. Bae, J.G. Kim, J.M. Park, W. Woo, S. Harjo, H.S. Kim, Scr. Mater. 165 (2019) 60–63.
[51] S. Lee, S.J. Lee, S.S. Kumar, K. Lee, B.C. De Cooman, Metall. Mater. Trans. A 42 (2011) 3638–3651.
[52] H. Li, S. Gao, Y. Tomota, S. Ii, N. Tsuji, T. Ohmura, Acta Mater. 206 (2021) 116621.
[53] A.J. Bogers, W.G. Burgers, Acta Metall. 12 (1964) 255–261.
[54] Z. Li, C.C. Tasan, K.G. Pradeep, D. Raabe, Acta Mater. 131 (2017) 323–335.
[55] W. Chen, X. An, Z. Wang, Y. Li, J. Gu, M. Song, J. Alloy. Compd. 883 (2021) 160876.
[56] Z. Li, F. Körmann, B. Grabowski, J. Neugebauer, D. Raabe, Acta Mater. 136 (2017) 262–270.
[57] J. Su, D. Raabe, Z. Li, Acta Mater. 163 (2019) 40–54.
[58] Z. Li, K.G. Pradeep, Y. Deng, D. Raabe, C.C. Tasan, Nature 534 (2016) 227–230.
[59] Z. Li, C.C. Tasan, H. Springer, B. Gault, D. Raabe, Sci. Rep. 7 (2017) 1316.